

On the role of return to isotropy in wall-bounded turbulent flows with buoyancy

Elie Bou-Zeid^{1,†}, Xiang Gao², Cedrick Ansoorge³ and Gabriel G. Katul⁴

¹Department of Civil and Environmental Engineering, Princeton University, Princeton, NJ 08544, USA

²Department of Mechanical and Aerospace Engineering, Princeton University, Princeton, NJ 08544, USA

³Institute for Geophysics and Meteorology, University of Cologne, 50969 Cologne, Germany

⁴Nicholas School of the Environment, Box 80328, Duke University, Durham, NC 27708, USA

(Received 22 February 2018; revised 17 August 2018; accepted 22 August 2018;
first published online 28 September 2018)

High Reynolds number wall-bounded turbulent flows subject to buoyancy forces are fraught with complex dynamics originating from the interplay between shear generation of turbulence (S) and its production or destruction by density gradients (B). For horizontal walls, S augments the energy budget of the streamwise fluctuations, while B influences the energy contained in the vertical fluctuations. Yet, return to isotropy remains a tendency of such flows where pressure–strain interaction redistributes turbulent energy among all three velocity components and thus limits, but cannot fully eliminate, the anisotropy of the velocity fluctuations. A reduced model of this energy redistribution in the inertial (logarithmic) sublayer, with no tuneable constants, is introduced and tested against large eddy and direct numerical simulations under both stable ($B < 0$) and unstable ($B > 0$) conditions. The model links key transitions in turbulence statistics with flux Richardson number (at $Ri_f = -B/S \approx -2, -1$ and -0.5) to shifts in the direction of energy redistribution. Furthermore, when coupled to a linear Rotta-type closure, an extended version of the model can predict individual variance components, as well as the degree of turbulence anisotropy. The extended model indicates a regime transition under stable conditions when Ri_f approaches $Ri_{f,max} \approx +0.21$. Buoyant destruction B increases with increasing stabilizing density gradients when $Ri_f < Ri_{f,max}$, while at $Ri_f \geq Ri_{f,max}$ limitations on the redistribution into the vertical component throttle the highest attainable rate of buoyant destruction, explaining the ‘self-preservation’ of turbulence at large positive gradient Richardson numbers. Despite adopting a ‘framework of maximum simplicity’, the model results in novel and insightful findings on how the interacting roles of energy redistribution and buoyancy modulate the variance budgets and the energy exchange among the components.

Key words: atmospheric flows, buoyant boundary layers, stratified turbulence

[†] Email address for correspondence: ebouzeid@princeton.edu

1. Introduction

Simultaneous shear and buoyancy are ubiquitous in many engineering and geophysical turbulent flows such as density-driven boundary layers in the ocean (Keitzl, Mellado & Notz 2016), air flow over land surfaces and ice sheets (Fernando & Weil 2010; Katul, Konings & Porporato 2011; Mahrt 2014) and flows in heat exchangers (You, Yoo & Choi 2003). Buoyancy complicates the flow dynamics beyond the well-studied canonical turbulent boundary layer, resulting in a rich set of persistent intellectual challenges. The ratio of the buoyant to inertial forces can be computed to assess their relative roles. This ratio is usually denoted as a Richardson number (Ri), many formulations exist as detailed for example in Stull (1988)). An $Ri = 0$ indicates no buoyancy effect, while a very large Ri magnitude indicates a buoyancy-dominated flow. Buoyancy can either augment turbulence generation in unstable flows ($Ri < 0$) (Chauhan *et al.* 2012; Salesky, Chamecki & Bou-Zeid 2017), or transfer turbulent kinetic energy (TKE) into potential energy associated with the variance of the density field in stable flows ($Ri > 0$) (Zilitinkevich 2002; Karimpour & Venayagamoorthy 2015; Venayagamoorthy & Koseff 2016). In the two limits where buoyancy dominates, $Ri \ll 0$ indicates a regime of natural (free) convection (Mellado 2012), while laminarization (full or intermittent as shown in Ansorge & Mellado (2014), Mahrt (2014), Shah & Bou-Zeid (2014a)) can occur when $Ri \gg 0$. The transitions with Ri between these two limiting stability regimes are nonlinear in terms of the influence on turbulence intensity and variance isotropy, and on the structural characteristics of eddies (i.e. their evolution from pancake-like horizontal motions under very-stable conditions, to hairpins and hairpin packets under near-neutral stability, to thermals and plumes under free convection).

A hallmark of flows bounded by a horizontal wall is the misalignment of shear production of turbulence in the streamwise direction and buoyancy production or destruction in the wall-normal direction. The energy exchanges between the components and the complex feedbacks across various statistical moments of the velocity and density fields give rise to counter-intuitive results. Buoyancy simultaneously influences the TKE budget of the flow and the effectiveness of eddies in transporting heat and momentum (Li & Bou-Zeid 2011; Shah & Bou-Zeid 2014b). Furthermore, while buoyancy acts on the wall-normal component, numerical simulations confirm that its primary impact in statically stable flows is through the reduction in horizontal velocity-variance shear production that buoyancy instigates indirectly (Jacobitz, Sarkar & VanAtta 1997; Shah & Bou-Zeid 2014a).

How does buoyancy alter the energy exchanges between the different components, and what are the implications for the dynamics of wall-bounded turbulent flows are the questions that frame this work. In the next section, we will overview the basic model development, followed in § 3 by validation of the results and discussion of their key implications on buoyancy modulation of turbulence. In § 4, we extend the model using the simplest energy redistribution closure framework to further probe the role of the interaction between redistribution and buoyancy on variance budgets and anisotropy. We then conclude with a summary and discussion of the broader implications of the findings.

2. Reduced model development

The budget equations for the variances of individual turbulent velocity components reveal the exchange of kinetic energy through the ‘pressure redistribution’ terms. These terms, as their alternative ‘return to isotropy’ name indicates, nudge turbulence

towards an isotropic state where its kinetic energy would be equipartitioned among its three velocity components (the redistribution terms sum exactly to zero in incompressible flows and thus do not appear in the equation for the full TKE budget). However, when TKE production in one or two of the components dominate, the flow cannot reach such an isotropic state except at scales commensurate with the Kolmogorov microscale η_K (provided $\eta_K \ll$ than the Dougherty–Ozmidov scale (Dougherty 1961) so that the anisotropic influence of buoyancy at these small scales is negligible). The degree of anisotropy therefore depends on the interplay between the anisotropic production by shear or buoyancy and the effectiveness of the redistribution process that acts differently across scales of motion (Brugger *et al.* 2018). It is therefore reasonable to hypothesize that these return-to-isotropy terms encode significant information about the statistical and structural properties of the turbulent velocity, and how such properties are modulated by the shear-to-buoyancy balance encoded in Ri . Buoyancy damping or excitation of vertical velocity must be communicated by these terms to the horizontal directions.

A logical starting point is an idealized high Reynolds number flow that remains three-dimensional with finite TKE in all components. A statistically steady state is assumed, which in geophysical settings must be interpreted as steadiness over limited periods, e.g. 15–60 min in the lower atmosphere (Stull 1988; Salesky, Chamecki & Dias 2012). Over a horizontally homogeneous wall, the flow will also be statistically homogeneous over the streamwise and cross-stream directions, which for an incompressible flow also results in negligible mean vertical velocity. We will neglect the terms in the variance budgets that result from rotation (the Coriolis force) since they are of second-order importance (Stull 1988); the effect of the Coriolis force mainly manifests as a rotation of the mean flow. The vertical TKE-transport terms are significant in the viscous and buffer layers, and also potentially in the outer layer (Pope 2000), but if one is interested in the inertial sublayer (the logarithmic region), the transport terms are approximately one order of magnitude smaller than the production and dissipation terms and can be neglected in a reduced model (André *et al.* 1978; Pope 2000; Shah & Bou-Zeid 2014a; Momen & Bou-Zeid 2017). This assumption might break down under strong wall buoyancy flux or near the density inversion that typically delineates the top of the atmospheric boundary layer (Stull 1988; Garcia & Mellado 2014), but will be adopted here since it is reasonable in the logarithmic layer under a wide range of stabilities (see appendix A for a model derivation where these terms are retained). An important side note to highlight is that, unlike for kinetic energy, the transport of density (or equivalently potential temperature) fluctuations is usually not negligible, and as a result the production–dissipation balance does not apply to scalar variance (Karimpour & Venayagamoorthy 2015) and is not invoked here.

In summary, a high- Re planar–homogeneous steady flow with an equilibrium between TKE production (by shear and buoyancy) and dissipation (by viscosity and buoyancy) is postulated. Such an idealization is in fact quite routinely used in practice when interpreting measurements in the inertial turbulent sublayer in laboratory experiments or flux measurements in the all-important atmospheric surface layer, or when collapsing field experiments in the context of Monin–Obukhov similarity theory (MOST) (Monin & Obukhov 1954; Kader & Yaglom 1990; Foken 2006; Bou-Zeid *et al.* 2010; Ghannam *et al.* 2018; Li, Katul & Liu 2018). With these assumptions, the velocity half-variance budgets reduce to (Zilitinkevich 1973; Stull 1988):

$$-\overline{u'w'} \frac{\partial \bar{u}}{\partial z} + \frac{\overline{p'}}{\rho_r} \frac{\partial \bar{u}'}{\partial x} - \nu \overline{\left(\frac{\partial u'}{\partial x_j} \right)^2} = S + R_u - \varepsilon_u = 0, \quad (2.1)$$

$$\frac{p'}{\rho_r} \frac{\partial v'}{\partial y} - \nu \overline{\left(\frac{\partial v'}{\partial x_j} \right)^2} = R_v - \varepsilon_v = 0, \quad (2.2)$$

$$-\frac{g}{\rho_r} \overline{w' \rho'} + \frac{p'}{\rho_r} \frac{\partial w'}{\partial z} - \nu \overline{\left(\frac{\partial w'}{\partial x_j} \right)^2} = B + R_w - \varepsilon_w = 0. \quad (2.3)$$

Throughout, u , v , w indicate instantaneous velocity components in the streamwise (x), cross-stream (y) and vertical (z) directions, respectively; p is instantaneous pressure; ρ is density and ρ_r its reference value; and ν is kinematic viscosity. Instantaneous quantities are decomposed into their turbulent fluctuations, denoted by a prime, and their averaged states, denoted by an overbar, where averaging is performed over coordinates of statistical homogeneity. The symbols in the middle equations refer, in the same order, to the terms on the left-hand side. The first term on the left-hand side of (2.1) is shear production ($S > 0$), while in (2.3) the first term is buoyancy production ($B > 0$) or destruction ($B < 0$). The terms with p are pressure redistribution terms (denoted by R_u , R_v and R_w), and the last terms on the left-hand side are viscous dissipation rates (ε_u , ε_v and ε_w , all positive).

The dissipation is performed by viscosity acting on the smallest eddies commensurate in size to η_K . If Re is sufficiently high, the energy cascade dissipates the anisotropy injected at the largest scales, resulting in an approximately isotropic dissipation with

$$\varepsilon_u = \varepsilon_v = \varepsilon_w \quad \Rightarrow \quad \varepsilon_w + \varepsilon_v = 2\varepsilon_u. \quad (2.4)$$

Viscous-range isotropy might not be exact at moderate Re where the limited turnovers between the production and dissipation do not completely remove the signature of the large-scale anisotropy. An anisotropy factor could then be introduced to generalize the model. However, under sufficiently high Re and ‘far’ from any wall effect (i.e. outside the buffer layer), the difference between the three components of dissipation and their mean is less than 10% (Spalart 1988; Pope 2000) and is ignored here. Another potential source of viscous-range anisotropy is strong static stability at high Ri where the Dougherty–Ozmidov length scale decreases and could become $\sim \eta_K$ (Grachev *et al.* 2015; Li, Salesky & Banerjee 2016); this aspect will be analysed in future studies using direct numerical simulation data.

Equations (2.1)–(2.3) are combined with (2.4) to yield

$$B + R_w + R_v = 2S + 2R_u. \quad (2.5)$$

In addition, since the redistribution terms must sum to zero in an incompressible flow,

$$R_u + R_v + R_w = 0 \quad \Rightarrow \quad R_v + R_w = -R_u. \quad (2.6)$$

Replacing (2.6) into (2.5), dividing by S and noting that $-B/S = Ri_f$ yields

$$\frac{R_u}{S} = -\frac{2}{3} - \frac{1}{3} Ri_f. \quad (2.7)$$

In a similar fashion, equations (2.4)–(2.6) can be modified (writing $\varepsilon_u + \varepsilon_w = 2\varepsilon_v$ in (2.4) and $R_u + R_w = -R_v$ in (2.6)) to yield

$$\frac{R_v}{S} = \frac{1}{3} - \frac{1}{3} Ri_f. \quad (2.8)$$

Then, using $R_w = -R_u - R_v$ results in

$$\frac{R_w}{S} = \frac{1}{3} + \frac{2}{3} Ri_f. \quad (2.9)$$

Finally, the total TKE dissipation ε (the sum of the half-variance dissipations in all three components that is used to define $\eta_K = (v^3/\varepsilon)^{1/4}$) can be related to Ri_f by summing (2.1) to (2.3), and using (2.6), to obtain

$$\frac{\varepsilon_u + \varepsilon_v + \varepsilon_w}{S} = \frac{\varepsilon}{S} = 1 - Ri_f. \quad (2.10)$$

3. Validation and implications

Equations (2.7)–(2.10) constitute a basic ‘reduced model’ that describes how energy redistribution and dissipation change with Ri_f . Under neutral conditions where $Ri_f = 0$, the model assumptions and formulation are very similar to algebraic Reynolds stress models such as those proposed by Launder, Reece & Rodi (1975) (see also Pope (2000), § 11.9). In this neutral limit, the model predicts $R_u = -2S/3$ and $R_v = R_w = S/3$. This yields the expected result that two thirds of shear production in the u component is redistributed equally into the v and w components where they are dissipated via $\varepsilon_v = \varepsilon_w$, and that one third of shear production gets dissipated directly via ε_u . This outcome results in equal energy in the cross-stream and vertical components, which is not observed in wall-bounded flows (Stull 1988; Bou-Zeid, Meneveau & Parlange 2005) due to the influence of the mean shear and to the wall pressure-blockage effect (McColl *et al.* 2016) that is absent here. The effect of this wall blockage is to increase pressure ($p' > 0$) for descending parcels ($\partial w'/\partial z < 0$ since $w = 0$ at the wall), while decreasing pressure ($p' < 0$) for ascending parcels ($\partial w'/\partial z > 0$). Wall blockage thus consistently produces negative ($p'\partial w'/\partial z$) contributions, or reduces the magnitude of the positive contributions, and as a result reduces the magnitude of the average redistribution of energy into the w component, $\overline{p'\partial w'/\partial z} > 0$, below model predictions. The comparative influence of wall blockage relative to the influence of increasing shear in the vicinity of the wall is discussed in Launder *et al.* (1975).

To assess the impact of neglecting wall blockage and other assumptions, the redistribution terms normalized by shear production (2.7)–(2.9) are compared to results from large eddy simulation (LES) under unstable conditions ($Ri_f < 0$) and direct numerical simulation (DNS) under stable conditions ($Ri_f > 0$). The DNS and LES details, with further references, are respectively provided in appendices B and C. It is noted that (i) the pressure redistribution terms are difficult to measure experimentally (no such measurements have been reported in the literature) and thus simulations are the only avenue for estimating them, and (ii) due to subgrid-scale modelling in the LES, these computations are deemed less accurate than in DNS. For the LES and DNS, the vertical average of the redistribution terms and of Ri_f over the inertial sublayer (logarithmic or modified logarithmic if non-neutral) are taken for comparisons since this is the layer where our model assumptions hold and that is of most interest in high- Re flows. The three redistribution terms computed from the reduced model and from the simulations are compared in figure 1. Figure 1(a) is for strongly unstable conditions ($Ri_f < -1$) and shows that the model captures LES trends but with some discrepancies. Figure 1(b) is for moderately unstable to stable conditions ($-2 < Ri_f < 1$), where the model again reasonably reproduces LES trends, but the relative errors are larger than for the strongly unstable conditions. The

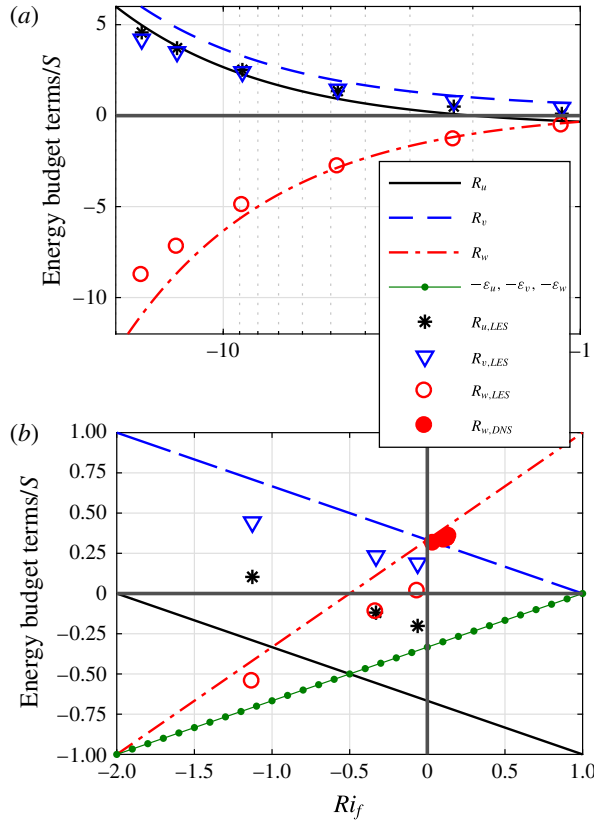


FIGURE 1. (Colour online) Variation of the variance budgets terms with stability: (a) for strongly unstable conditions, (b) for moderately unstable and stable conditions. Lines are from the reduced model; markers are determined from LES or DNS.

agreement with DNS is significantly better. These DNS were of rotating (Ekman) flows where the two horizontal-variance components are difficult to disentangle due to shear production in the cross-stream direction. Here, they are lumped and compared to $R_w = -R_u - R_v$, which are in better agreement relative to the match with LES results. It is not possible to ascertain whether the discrepancies between the model and LES are due to model simplifications and/or unavoidable errors in LES computations of the redistribution. Nonetheless, the model captures the leading-order physics of variance redistribution without resorting to tuneable coefficients, and can be used to further probe their impact on the structural characteristics of eddies and on turbulence regimes.

Focusing on the buoyancy influence on the budget terms in figure 1, the model and simulations both indicate apparent transitions in turbulence regimes at approximate Ri_f values, although with some discrepancy between the two as to the exact Ri_f at which a transition occurs. These regimes will henceforth be discussed in terms of the transition Ri_f values indicated by the model, but the reader must bear in mind the potential uncertainty in these model-derived values. Moreover, in other flow set-ups with shear and buoyancy such as a jet effluent into a stable environment or flow over inclined walls, the same turbulence regimes might emerge but the transition Ri_f values will likely be different from horizontal wall-bounded flows.

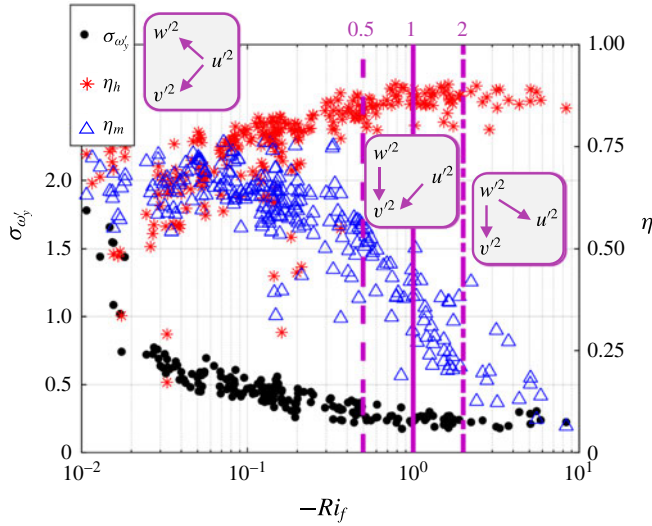


FIGURE 2. (Colour online) Standard deviation of the perturbation cross-stream vorticity, $\sigma_{\omega'_y}$, heat transport efficiency, η_h , and momentum transport efficiency, η_m , versus Ri_f . Vertical lines are at $Ri_f = -0.5$ (dashed), -1 (solid) and -2 (dot-dashed). Experiments and analysis methods are described in Li & Bou-Zeid (2011). Purple rectangles depict the directionality of energy transfer.

For the current configuration under unstable conditions, as Ri_f decreases from its zero neutral value where energy is redistributed from the u component into the v and w components, the following can be noted:

(i) At $Ri_f < -0.5$, R_w becomes negative, indicating a redistribution out of the vertical component $\overline{w^2}$. The streamwise component, however, remains a source and the cross-stream is now the only net recipient of energy. Furthermore, in the $\overline{u^2}$ budget, dissipation overtakes redistribution as the main sink. The regime transition indicated by the model at $Ri_f = -0.5$ can in fact be observed in very high Reynolds number atmospheric flows. One illustration is provided in figure 2, where the standard deviation of the cross-stream perturbation vorticity $\sigma_{\omega'_y}$ (where $\omega'_y = \partial u' / \partial z - \partial w' / \partial x$) and the heat η_h and momentum η_m transfer efficiencies measured in the atmosphere above a lake are featured. The efficiencies are defined as the net flux F of heat or momentum divided by the total downgradient flux from ejections and sweeps $\eta = F_{total} / F_{downgradient}$, as detailed in Li & Bou-Zeid (2011). At $Ri_f \approx -0.5$, the momentum transfer efficiency begins a rapid decline as the now buoyantly dominated vertical velocity starts to decorrelate from the horizontal component and vertical motions are no longer simply responding to horizontal ones. Furthermore, the decline in $\sigma_{\omega'_y}$, which encodes information about the structural characteristics of turbulent eddies, and the increase in η_h slow down. Thus, not only the turbulence energy, but also its structure is modified by buoyancy below this Ri_f as the vertical component is now dominated by buoyancy generation.

(ii) At $Ri_f < -1$, $|R_w| > |R_u|$ and the w component becomes the main supplier of energy in the redistribution interplay but R_u remains a source as well. The directionality of redistribution (indicated by arrows in figure 2) does not change at this Ri_f . However, turbulence eddy structure and statistics are altered as can be deduced from η_h , which plateaus beyond this value. This plateau suggests that buoyancy fully dominates the

generation of vertical velocity perturbations and their correlation with temperature perturbations, with no effect on heat transport from shear beyond this point.

(iii) At $Ri_f < -2$, there is a transition to $R_u > 0$ implying that $\overline{u^2}$ now becomes a net recipient of energy originating from $\overline{w^2}$. The flow can be considered buoyancy-dominated beyond this point since the streamwise fluctuations are now modulated by buoyantly generated energy. At this value of $Ri_f = -2$, one can note the onset of a new turbulence regime in figure 2 as η_m , η_h and σ_{ω_y} all reach a plateau.

On the stable side, as Ri_f increases from zero:

(iv) At $Ri_f > 0.25$, buoyancy destruction exceeds viscous dissipation in the budget of $\overline{w^2}$ ($\varepsilon_w/S < -B/S = Ri_f$), and beyond this point it dominates the damping and the structure of vertical fluctuations.

(v) At $Ri_f > 0.5$, buoyancy destruction exceeds the total TKE viscous dissipation in all components ε .

(vi) The $Ri_f = 1$ limit is forbidden. The dissipation and the redistribution to the v -component become zero requiring complete laminarization of the flow, while the model predicts $R_u = R_w$, requiring finite turbulent energy. This point is further examined below to show that a lower limit of $Ri_f \approx 0.21$ exists and that turbulence can be sustained at high stabilities (Ri_g values) provided Re remains high.

4. Extended model with linear Rotta closure

To proceed further in variance modelling, a linear Rotta-type closure for the redistribution term is introduced and is given by

$$R_u = -\frac{c\varepsilon}{k} \left(\overline{u^2} - \frac{2}{3}k \right) \quad R_v = -\frac{c\varepsilon}{k} \left(\overline{v^2} - \frac{2}{3}k \right) \quad R_w = -\frac{c\varepsilon}{k} \left(\overline{w^2} - \frac{2}{3}k \right), \quad (4.1a-c)$$

where $k = 0.5(\overline{u^2} + \overline{v^2} + \overline{w^2})$ is the TKE and c is a model constant. The ratio k/ε represents a characteristic decay time of the turbulence, which here encodes the time required to redistribute variance between components. This model captures the ‘slow’ part of the redistribution and represents the simplest closure one can propose for the return-to-isotropy terms. More detailed models that include the effect of shear and wall blockage, buoyancy and potentially other physical processes, on the pressure–strain correlations have been proposed and used (Canuto *et al.* 2001; Heinze, Mironov & Raasch 2016). However, to assess the limits of the simplest plausible formulation (and to avoid including other budget equations in the model), we will focus on the linear Rotta closure in this study.

4.1. Model prediction for velocity variances

Inserting the expressions of (4.1) into (2.7)–(2.9), and using $S/\varepsilon = (1 - Ri_f)^{-1}$, yields

$$\frac{\overline{u^2}}{k} = \frac{S}{c\varepsilon} \left(\frac{2}{3} + \frac{1}{3}Ri_f \right) + \frac{2}{3} = \frac{1}{3c} \left(\frac{2 + Ri_f}{1 - Ri_f} \right) + \frac{2}{3}, \quad (4.2)$$

$$\frac{\overline{v^2}}{k} = \frac{S}{c\varepsilon} \left(-\frac{1}{3} + \frac{1}{3}Ri_f \right) + \frac{2}{3} = \frac{1}{3c} \left(\frac{-1 + Ri_f}{1 - Ri_f} \right) + \frac{2}{3} = -\frac{1}{3c} + \frac{2}{3}, \quad (4.3)$$

$$\frac{\overline{w^2}}{k} = \frac{S}{c\varepsilon} \left(-\frac{1}{3} - \frac{2}{3}Ri_f \right) + \frac{2}{3} = \frac{1}{3c} \left(\frac{-1 - 2Ri_f}{1 - Ri_f} \right) + \frac{2}{3}. \quad (4.4)$$

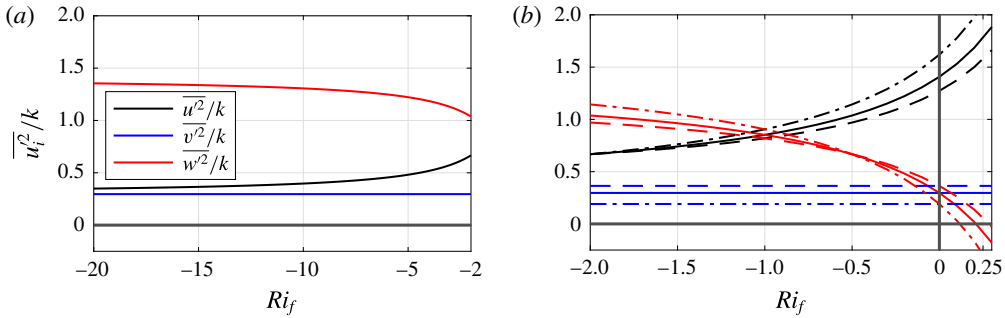


FIGURE 3. (Colour online) Variance to TKE ratios predicted by the model as a function of Ri_f : dot–dash lines with $c = 0.7$, solid lines with $c = 0.9$ and dashed line with $c = 1.1$.

These model variances are shown in figure 3 using $c = 0.9$ (solid lines), which has been reported as optimal in closure modelling (Pope 2000). The $c = 0.9$ (or 1.8 in the full-variance budget) has some theoretical justification (Katul *et al.* 2013) for neutral flows as well. A notable prediction of the model is that the fraction $\overline{v^2}/k$ remains independent of stability at a value of approximately 0.3, and this is indeed supported by the LES results (not plotted here) where $\overline{v^2}/k \approx 0.25\text{--}0.35$ at heights $z > \delta/4$, where δ is the total flow depth. The ratio is higher closer to the wall, but the dependence on stability in the LES runs is weak and non-monotonic.

Under neutral conditions where $Ri_f = 0$ and with $c = 0.9$, equations (4.2)–(4.4) yield $\overline{u^2}/k = 1.41$ and $\overline{v^2}/k = \overline{w^2}/k = 0.3$, which are reasonably close to values observed in measurements and numerical simulations in the logarithmic region away from the wall (e.g. Bou-Zeid *et al.* (2005)), although as discussed before $\overline{v^2}/k > \overline{w^2}/k$. On the other hand, under very strongly unstable conditions when $-Ri_f \gg 1$ and production is dominated by buoyancy, $\overline{u^2}$ and $\overline{w^2}$ reverse roles, and $\overline{w^2}/k = 1.41$ while $\overline{u^2}/k = \overline{v^2}/k = 0.3$ as can be seen in figure 3(a) at the free convection limit of $Ri_f \ll 0$. The anisotropy of the variance ratios asymptotes to $\overline{w^2}/\overline{v^2} \approx \overline{w^2}/\overline{u^2} \approx 4.6$. These values are close to the ≈ 3.2 reported for DNS of free convection above a heated plate by Mellado (2012), and to the ≈ 3.4 of Salesky *et al.* (2017) at the lowest Ri_f they studied using LES. The better predictions of the model in the free convection limit, compared to the neutral limit, are not surprising since the energy is being injected in the vertical component and the redistributions to the horizontal components must become equal. This is indicated by the reduced model and the LES in figure 1 and is expected since physically these directions are exactly similar in that limit: the wall effect does not hinder energy redistribution into either horizontal receiving components.

Under stable conditions, a maximum attainable flux Richardson number ($Ri_{f,max}$) emerges beyond which $\overline{w^2} < 0$ (figure 3b). This $Ri_{f,max}$ ($= 0.21$ for $c = 0.9$) cannot be exceeded because when it is approached, $\overline{w^2}$ approaches zero and buoyancy destruction ($\sim \overline{w\theta'}$) will be throttled by the rate of redistribution R_w , maintaining $Ri < Ri_{f,max}$. That is, the constraint of $\overline{w^2} > 0$ limits the maximum attainable R_w according to (4.1) (it will be the R_w attained when $\overline{w^2} \rightarrow 0$). This maximum R_w then limits the highest attainable energy flux into the vertical component, which must simultaneously limit the buoyant energy destruction in that component (via budget (2.3)). Thus, pressure redistribution of variance from the streamwise to the vertical velocity component becomes the primary regulator of turbulence regime at

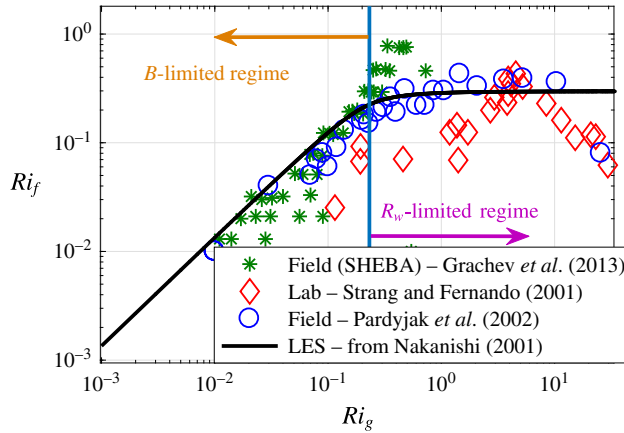


FIGURE 4. (Colour online) Flux versus gradient Richardson numbers from laboratory and atmospheric field experiments, data from Katul *et al.* (2014).

this asymptotic $Ri_{f,max}$. This limiting value of ≈ 0.21 is quite consistent with previous estimates (ranging from 0.19 to 0.21) based on second-order moments models that make comparable assumptions to the ones we make here (Yamada 1975; Mellor & Yamada 1982), as well as with the asymptotic limit of Ri_f that can be obtained from its relation to the empirically determined Monin–Obukhov gradient stability correction functions (Wyngaard 2010, p. 281). The exact limiting value however might not be 0.21 if buoyancy or other factors (waves, wall-blockage, laminarization, intermittency, non-stationarity, etc.) alter the redistribution efficiency and consequently the value of c . To account for this possibility and to investigate the change in variances with uncertainties in c , figure 3(b) presents the profiles with c values of 0.7 and 1.1. The attainable $Ri_{f,max}$ limit is reduced to approximately 0.12 for $c = 0.7$ and increased to about 0.28 when $c = 1.1$. From (4.4), one can derive (again by constraining $\overline{w^2}$ to remain > 0) the following expression for the dependence on c of this asymptotic flux Richardson number as $Ri_{f,max} = (c - 0.5)/(c + 1)$, which increases with increasing c . That is, the more efficient the redistribution (higher c), the higher the attainable $Ri_{f,max}$ since a high redistribution can sustain a higher buoyancy destruction rate. The limit of $Ri_{f,max} \approx 0.25$, consistent with the classic estimate from linear stability analysis (Miles & Howard 1964) requires $c = 1$, although we must point out that their result was derived for a bulk Ri .

Atmospheric boundary layer field experiments corroborate the model findings: values of $Ri_f > \approx 0.21$ are atypical. Gradient and flux Richardson numbers are about equal and vary together between $0 < Ri_f \approx Ri_g < 0.21$; however, beyond this point, Ri_f reaches a plateau at $Ri_{f,max} \approx 0.21$ while Ri_g continues to increase (Katul *et al.* 2014; van Hooijdonk *et al.* 2018). This is illustrated in figure 4 where the demarcation between the buoyancy-destruction limited and the redistribution-limited regimes is indicated. Thus, even at higher bulk stabilities, the redistribution throttle mitigates the continuous increase in buoyant destruction and the collapse of turbulence (until the Dougherty–Ozmidov length scale approaches η_K (Katul *et al.* 2014)). A further evidence of the physical significance of this Ri_f limit is that the spectrum of measured vertical velocity above an extensive ice sheet no longer exhibits an inertial subrange when Ri_f exceeds a threshold estimated at ≈ 0.25 (Grachev *et al.* 2013).

Another conclusion that can be drawn from the analysis of the relation between $Ri_{f,max}$ and c is that the value of c must be constrained to $c > 0.5$ (otherwise $Ri_{f,max}$ in stable flows cannot be > 0) and $c < 2.5$ (otherwise $Ri_{f,max} > 1$). As discussed above, $Ri_{f,max} > 1$ cannot be attained when a high- Re flow is stationary, planar-homogeneous and lacking a mean vertical velocity. For the aforementioned conditions, $Ri_{f,max} > 1$ results in a negative TKE dissipation rate (i.e. viscous production).

4.2. Model prediction for velocity anisotropy, and the implied Rotta constant

As detailed in the introduction, return to isotropy is a trend, but the turbulence remains anisotropic if production is dominated by one or two components. One important question that emerges is to what degree can return to isotropy succeed in equi-partitioning the energy, and how does buoyancy influence this equi-partitioning. The flow anisotropy is best characterized by the velocity anisotropy tensor

$$b_{ij} = \frac{u'_i u'_j}{2k} - \frac{\delta_{ij}}{3}. \quad (4.5)$$

Based on (4.2)–(4.4), the diagonal components of this tensor can be modelled as

$$b_{11} = \frac{1}{6c} \left(\frac{2 + Ri_f}{1 - Ri_f} \right), \quad (4.6)$$

$$b_{22} = -\frac{1}{6c}, \quad (4.7)$$

$$b_{33} = \frac{1}{6c} \left(\frac{-1 - 2Ri_f}{1 - Ri_f} \right), \quad (4.8)$$

where the index 1 denotes the streamwise direction, 2 the cross-stream and 3 the vertical. Under neutral conditions and with $c = 0.9$, this results in $b_{11} = (3c)^{-1} = 0.37$ and $b_{22} = b_{33} = (-6c)^{-1} = -0.185$ (they sum to zero). These parameters are reported widely in the literature on neutral homogeneous shear flows; they depend on the Reynolds number as well as the shear rate (Pumir 1996; Briard *et al.* 2016). The values obtained here are within the reported ranges; specifically, at the highest simulated shear rate, Isaza & Collins (2009) found $b_{11} \approx 0.38$, $b_{22} \approx -0.12$ and $b_{33} \approx -0.26$ (notice the 22 and 33 notations in their paper are the inverse of ours). It is to be noted that their simulations were of homogeneous neutral free shear and hence there were no wall or buoyancy; therefore, the asymmetry between the cross-stream and vertical components is due to the effect of shear on the vertical component. The effect of shear is in fact broadly similar to the effect of a wall: it would reduce redistribution to the shear-normal vertical component and result in $b_{33} < b_{22}$ (both negative) or equivalently $\overline{w'^2} < \overline{v'^2}$. That is, the presence of a wall or the influence of shear alter the redistribution and require a modification of the simplest linear Rotta model, and this modification due to shear is in fact often included as the second term in redistribution closure schemes (e.g. Canuto *et al.* 2001).

Some studies (Gerz, Schumann & Elghobashi 1989; Holt, Koseff & Ferziger 1992) also examined b_{11} , b_{22} and b_{33} under non-neutral conditions. The direct measurement from simulations can be compared to predictions of the present model but the influence of buoyancy on redistribution and on the value of the Rotta constant needs to be accounted for example, as in Canuto *et al.* (2001). An alternative approach is in fact to use the present model of the components of the velocity anisotropy tensor

(or the variances or variance differences that can also be derived from (4.2) to (4.4)) to estimate the Rotta model constant and how it varies with stability. Such estimates of c , while possible in principle, proved difficult. They are highly sensitive to the accuracy of the computed or measured variances near Ri_f values that would cause the numerators or denominators of (4.6)–(4.8) to approach 0. Computations from DNS for example suggest a reasonable value of c that varies between 0.8 and 1.3, but with no clear trend with increasing stability. As such, while this paper establishes the influence of redistribution of energy on buoyancy modulation of turbulent flows, the influence of buoyancy on redistribution is a topic that requires further investigation.

5. Conclusion

A novel perspective on the role energy redistribution plays in wall-bounded flows with buoyancy has been unfolded through a reduced model based on the budgets of the half-variances of the three velocity components. The model makes assumptions that are commonly used in turbulence closure and modelling including stationarity, horizontal homogeneity and production–dissipation equilibrium, hence postulating that vertical energy transport is of secondary importance (though the model can be extended to include transport terms as illustrated in appendix A). The model is hence not applicable near strong density inversions that might exist in geophysical flows. On the other hand, the framework is applicable in the inertial sublayer (logarithmic zone) of wall-bounded flows (between the buffer and outer layers) that extends from a few millimetres to over 100 m in the atmosphere and is therefore of very high relevance. More generally, the model is also applicable, with appropriate modifications, to other similar flows where the assumptions (mainly local TKE production–destruction balance) are satisfied, such as some free shear configurations and flows over inclined heated/cooled walls.

The basic model (2.7)–(2.10) has no tuneable coefficient, while its extended version (4.1)–(4.4) only requires knowledge of the well-studied Rotta constant for the closure of the redistribution terms. Despite this simplicity, the model predictions are far reaching and compare reasonably well with DNS, LES or observational data in terms of energy redistribution variation with Ri_f , cross-stream velocity-variance independence of stability and the asymptotic anisotropy under free convective conditions. The model also elucidates how the redistribution of energy modulates the influence of stability on the flow. When buoyancy generates turbulence, redistribution controls the transition from a shear-dominated flow at $Ri_f > \approx -0.5$ (vertical component receives energy from streamwise component), to a buoyancy-dominated regime at $Ri_f < \approx -2$ (vertical component dominates and transfers energy to the streamwise component). Under stable conditions, the reduced model yields a realizability constraint of $Ri_{f,max} \approx 0.21$. This constraint is related to the limitations on the redistribution of energy from the streamwise to the vertical component that throttle the maximum attainable buoyant destruction to approximately 21% of shear production. This explains the ‘self-preservation’ of turbulence at large positive gradient Richardson numbers, as well as the origin and magnitude of the much discussed $Ri_{f,max}$. In addition, the linkage in the extended model of the redistribution and the standard Rotta closure offers novel constraints on the Rotta constant $0.5 < c < 2.5$. The model hence not only successfully explains some very-broadly observed statistical and structural properties of turbulence at high Reynolds numbers and how they vary with buoyancy, but it also extends the boundaries of our current understanding of the physics and ability to close and simulate turbulent dynamics.

More broadly, the primary implication of the study is that pressure redistribution, by controlling the communication between the variance components, can explain a significant range of empirically observed turbulent flow dynamics. These return-to-isotropy terms have been much less studied than other terms in the budget equations, partially because they are not yet measurable experimentally, but their physics and relevance warrant more investigations and the model developed here can serve as ‘framework of maximum simplicity’ in these efforts.

Acknowledgements

This work is supported by the Princeton Environmental Institute’s Grand Challenges Program. The authors would also like to thank Professor D. Li for providing the data used in figure 2, as well as the anonymous reviewers for their constructive and thoughtful suggestions. G.G.K. acknowledges partial support from the National Science Foundation (NSF-EAR-1344703, NSF-AGS-1644382, NSF-IOS-1754893, and NSF-DGE-1068871). C.A. acknowledges support through Project C7 of the DFG’s Trans-regional Research Collaborative and a UoC PostDoc Grant.

Appendix A. The potential role of transport

The potential role of transport can be investigated using a modified version of the basic reduced model. If the transport terms denoted by T_u , T_v and T_w , which lump the turbulent, pressure and viscous transports, are retained, the half-variance budget equations become (Zilitinkevich 1973)

$$S + T_u + R_u - \varepsilon_u = 0, \quad (\text{A } 1)$$

$$T_v + R_v - \varepsilon_v = 0, \quad (\text{A } 2)$$

$$B + T_w + R_w - \varepsilon_w = 0. \quad (\text{A } 3)$$

Using the same derivation as in the main text, the model results can be generalized to:

$$\frac{R_u}{S} = -\frac{R_{if}}{3} - \frac{2}{3} + \frac{1}{3} \frac{T_w + T_v - 2T_u}{S}, \quad (\text{A } 4)$$

$$\frac{R_v}{S} = -\frac{R_{if}}{3} + \frac{1}{3} + \frac{1}{3} \frac{T_u + T_w - 2T_v}{S}, \quad (\text{A } 5)$$

$$\frac{R_w}{S} = \frac{2}{3} R_{if} + \frac{1}{3} - \frac{1}{3} \frac{2T_w - T_v - T_u}{S}. \quad (\text{A } 6)$$

The degree to which these transport terms influence the dynamics depends on whether they partially cancel each other or add up. One can note for example that if they are all equal (with the same sign), the net transport terms in (A 4)–(A 6) will be exactly zero. These transport terms will be more significant under unstable conditions, which might explain the larger discrepancies under such conditions (figure 1) than in stable regimes. Another effect of stability is to increase the effective Re , defined as a scale separation between the largest and the dissipative scales, under unstable conditions. This will result in a smaller (larger) Kolmogorov scale under unstable (stable) conditions, resulting in a larger (smaller) number of cascading steps to wipe out anisotropy. Nonetheless, the model compares better to the stable DNS data. These aspects will be further examined in future studies.

	re_{high}	ri000	ri014	ri029	ri058	ri076	ri114
$Re/10^3$	45	26	26	26	26	26	26
δ^+	2365	1400	1370	1200	1120	1180	1110
Ri_B	0	0	0.14	0.29	0.58	0.76	1.14
Case used for initialization	n/a	n/a	ri000	ri000	ri014	ri058	ri076
t_{start}^-	n/a	n/a	0.0	0.0	0.57	1.18	1.64
$t_{analysis-start}^-$	n/a	n/a	1.5	0.47	1.02	1.48	2.12
t_{end}^-	n/a	n/a	1.66	0.62	1.18	1.64	2.28

TABLE 1. DNS cases for Ekman flow. Grids are $2560 \times 640 \times 5120$ for case re_{high} and $3072 \times 512 \times 6144$ for all other cases in streamwise/vertical/cross-stream direction. The streamwise direction of the simulations is rotated by 20.5° with respect to the geostrophic wind to achieve approximate alignment with the surface stress (for analysis, the data are considered in an exactly shear-stress-aligned coordinate system).

Appendix B. Description of direct numerical simulations (DNS) of stable flows

The Ekman layer cases are studied by direct numerical simulation (DNS). The set-up and data used here are identical to those in Ansorge & Mellado (2016), extended by the two more stable cases ri076, ri114 (table 1). Governing flow equations are solved numerically in a non-dimensional framework under the Boussinesq approximation, and boundary conditions correspond to a horizontally periodic Ekman flow over a smooth wall and with a fixed temperature difference between the wall and the free stream. Parameters of this set-up are the geostrophic wind velocity G , the fluid kinematic viscosity ν , the Coriolis parameter f and the buoyancy difference B_0 between the wall and free stream. We let G be the free-stream geostrophic forcing and $u_* = \sqrt{\|\tau\|/\rho}$ the friction velocity. For analysis, the coordinate x is rotated to coincide with the direction of the negative surface shear stress τ , i.e. the flow is investigated in shear-aligned coordinates in analogy to a channel-flow configuration. The non-dimensional parameters governing the flow set-up are a Reynolds number $Re = G^2/(f\nu)$ that sets the turbulence scale separation of the problem and a bulk Richardson number $Ri_B = G\delta_{neutral}/B_0$ describing the stratification in terms of the Buoyancy jump and the boundary layer depth scale under neutral conditions. The turbulent scale separation is given in terms of the boundary layer depth scale in wall units $\delta^+ = u_*^2/(f\nu)$. Times are given as fraction of the inertial period, i.e. $t^- = tf/2\pi$ and time averaging is denoted by an overbar.

A list of DNS cases is given in table 1. The initial condition used for the cases ri014 and ri029 is a realization of the neutrally stratified case ri000, and the buoyancy profile is prescribed by an error function in the wall-normal direction. The stronger stratified cases ri058, ri076 and ri114 use the final states of cases ri014, ri058 and ri076 respectively as initial condition with the buoyancy field adjusted by multiplication with a scalar to match the required Ri_B . Data are averaged over the period between $t_{analysis-start}^- \leq t^- \leq t_{end}^-$ (see table 1) to minimize the effect on the analysis of initial adaptations to instantaneous temperature forcing at the bottom (cf. Ansorge & Mellado (2014)).

Appendix C. Description of the large eddy simulations (LES) for unstable flows

The details of the LES code are provided in Bou-Zeid, Meneveau & Parlange (2004), Bou-Zeid *et al.* (2005), and for simulations with buoyancy, further details

Simulation number	$\langle w'T' \rangle$ (K m s ⁻¹)	Ri_{f0}	$N_{x,y,z}$	z_i/L	L_z (m)	L (m)	Imposed inversion base height (m)
1	0	0	256 ³	0	1000	∞	No inversion
2	0.0125	-0.0363	256 ³	-6.81	1500	-146.9	800
3	0.025	-0.0725	256 ³	-12.82	1500	-78.0	800
4	0.05	-0.1459	256 ³	-23.42	1500	-42.7	800
5	0.1	-0.2916	256 ³	-40.65	1500	-24.6	800
6	0.2	-0.5590	256 ³	-65.79	1500	-15.2	800
7	0.3	-0.8136	256 ³	-85.47	1500	-11.7	800

TABLE 2. Simulation parameters for the turbulent boundary layers. Ri_{f0} is the surface flux Richardson number $Ri_{f0} = -g/\theta_0 \langle w'\theta' \rangle / (\langle u'w' \rangle \partial \langle u \rangle / \partial z)$, where g is the gravitational acceleration, θ is temperature and θ_0 its reference value, angle brackets denote Reynolds averaging and the other variables are as defined in the main text. $N_{x,y,z}$ is the number of the grid nodes, $z_i = 800$ m is the height of the inversion base in all unstable simulations, L_z is the domain height and L is the Obukhov length. The non-dimensional time step in all simulations is set to $dt = u_* / L_z = 10^{-5}$.

are provided in Huang & Bou-Zeid (2013), Shah & Bou-Zeid (2014b); and Momen & Bou-Zeid (2017). The code solves the continuity, Navier–Stokes, and heat budget equations for a Boussinesq fluid using a pseudo-spectral method for computing horizontal derivatives and for the test filtering required by the dynamic subgrid-scale (SGS) model. Doubly periodic boundary conditions are hence used in the horizontal directions. A second-order centred difference scheme is used in the vertical direction, requiring a staggered grid. A second-order Adams–Bashforth scheme is used for the time integration. The deviatoric part of the SGS stress tensor is modelled using the scale-dependent Lagrangian dynamic model, where a sharp spectral cutoff filter is used (Bou-Zeid *et al.* 2005). Explicit filtering at twice and four times the grid scales is needed for this scale-dependent dynamic approach. At the bottom of the domain ($z = 0$), the vertical velocity is set to 0. Since a staggered grid is used, no boundary conditions are needed for the horizontal velocities at the surface. Instead, the stresses associated with vertical fluxes of horizontal momentum are needed; they are modelled through a log-law based equilibrium wall model (Moeng 1984) for the neutral case, with a MOST correction for the unstable or stable cases; a roughness length corresponding to a hydrodynamically rough wall is used in the wall model. Velocities test filtered at twice the grid scale (Bou-Zeid *et al.* 2005) are used to obtain an average stress over the wall that is close to the stress obtained from the log law or MOST prediction. In non-neutral simulations conducted for this study, a constant surface heat flux is imposed to produce different static stability conditions. In these simulations, the dimensional surface heat flux $\langle w'T' \rangle$ varies from 0.0125 to 0.3 (i.e. 0.0125, 0.025, 0.05, 0.1, 0.2, 0.3) K ms⁻¹, which are typical values observed in field measurements of atmospheric flow over ground surfaces. A stress-free lid condition (i.e. a zero vertical velocity and zero shear stress boundary condition) is imposed at the top of the domain so that the flow corresponds to a half-channel flow with an impermeable centreline (since the Coriolis force is not included). In the unstable cases, the computational domain is larger than the initial boundary layer thickness to enable the atmospheric boundary layer to grow without interacting with the top boundary. In addition, we impose a strong thermal inversion below the

top of the computational domain to slow the growth of the boundary layer since with a constant heat flux into the system at the bottom, the boundary layer would keep growing if there are no Coriolis forces. In all of the simulations, the flows are pressure-driven (i.e. forced by a pressure gradient in the streamwise direction), and the pressure gradient balances the surface shear stress under steady-state conditions. The applied pressure forcing hence determines the kinematic wall stress $u_*^2 = \sqrt{\tau_{13}^2 + \tau_{23}^2}$, where τ_{13} and τ_{23} are the stresses at the surface, and the corresponding friction velocity u_* is used to normalize velocities. The length scale we use in normalizations is the nominal boundary layer thickness $\delta = 1000$ m, but the top inversion starts at $z_i = 800$ m. A time scale can then be defined using δ and u_* ; all simulation results are normalized with these scales. The simulation parameters are given in table 2.

REFERENCES

- ANDRÉ, J. C., DE MOOR, G., LACARRÈRE, P. & DU VACHAT, R. 1978 Modeling the 24-hour evolution of the mean and turbulent structures of the planetary boundary layer. *J. Atmos. Sci.* **35** (10), 1861–1883.
- ANSORGE, C. & MELLADO, J. P. 2014 Global intermittency and collapsing turbulence in the stratified planetary boundary layer. *Boundary-Layer Meteorol.* **153** (1), 89–116.
- ANSORGE, C. & MELLADO, J. P. 2016 Analyses of external and global intermittency in the logarithmic layer of Ekman flow. *J. Fluid Mech.* **805**, 611–635.
- BOU-ZEID, E., HIGGINS, C., HUWALD, H., MENEVEAU, C. & PARLANGE, M. B. 2010 Field study of the dynamics and modelling of subgrid-scale turbulence in a stable atmospheric surface layer over a glacier. *J. Fluid Mech.* **665**, 480–515.
- BOU-ZEID, E., MENEVEAU, C. & PARLANGE, M. B. 2004 Large-eddy simulation of neutral atmospheric boundary layer flow over heterogeneous surfaces: blending height and effective surface roughness. *Water Resour. Res.* **40** (2), W02505.
- BOU-ZEID, E., MENEVEAU, C. & PARLANGE, M. B. 2005 A scale-dependent Lagrangian dynamic model for large eddy simulation of complex turbulent flows. *Phys. Fluids* **17** (2), 25105.
- BRIARD, A., GOMEZ, T., MONS, V. & SAGAUT, P. 2016 Decay and growth laws in homogeneous shear turbulence. *J. Turbul.* **17** (7), 699–726.
- BRUGGER, P., KATUL, G. G., DE ROO, F., KRÖNIGER, K., ROTENBERG, E., ROHATYN, S. & MAUDER, M. 2018 Scalewise invariant analysis of the anisotropic Reynolds stress tensor for atmospheric surface layer and canopy sublayer turbulent flows. *Phys. Rev. Fluids* **3** (5), 054608.
- CANUTO, V. M., HOWARD, A., CHENG, Y. & DUBOVIKOV, M. S. 2001 Ocean turbulence. Part I: one-point closure model – momentum and heat vertical diffusivities. *J. Phys. Oceanogr.* **31** (6), 1413–1426.
- CHAUHAN, K., HUTCHINS, N., MONTY, J. & MARUSIC, I. 2012 Structure inclination angles in the convective atmospheric surface layer. *Boundary-Layer Meteorol.* **147** (1), 41–50.
- DOUGHERTY, J. P. 1961 The anisotropy of turbulence at the meteor level. *J. Atmos. Terr. Phys.* **21** (2), 210–213.
- FERNANDO, H. J. S. & WEIL, J. C. 2010 Whither the stable boundary layer? *Bull. Am. Meteorol. Soc.* **91** (11), 1475–1484.
- FOKEN, T. 2006 50 years of the Monin–Obukhov similarity theory. *Boundary-Layer Meteorol.* **119** (3), 431–447.
- GARCIA, J. R. & MELLADO, J. P. 2014 The two-layer structure of the entrainment zone in the convective boundary layer. *J. Atmos. Sci.* **71** (6), 1935–1955.
- GERZ, T., SCHUMANN, U. & ELGHOBASHI, S. 1989 Direct numerical-simulation of stratified homogeneous turbulent shear flows. *J. Fluid Mech.* **200**, 563–594.
- GHANNAM, K., KATUL, G. G., BOU-ZEID, E., GERKEN, T. & CHAMECKI, M. 2018 Scaling and similarity of the anisotropic coherent eddies in near-surface atmospheric turbulence. *J. Atmos. Sci.* **75** (3), 943–964.

- GRACHEV, A. A., ANDREAS, E. L., FAIRALL, C. W., GUEST, P. S. & PERSSON, P. O. G. 2013 The critical Richardson number and limits of applicability of local similarity theory in the stable boundary layer. *Boundary-Layer Meteorol.* **147** (1), 51–82.
- GRACHEV, A. A., ANDREAS, E. L., FAIRALL, C. W., GUEST, P. S. & PERSSON, P. O. G. 2015 Similarity theory based on the Dougherty–Ozmidov length scale. *Q. J. R. Meteorol. Soc.* **141** (690), 1845–1856.
- HEINZE, R., MIRONOV, D. & RAASCH, S. 2016 Analysis of pressure-strain and pressure gradient-scalar covariances in cloud-topped boundary layers: a large-eddy simulation study. *J. Adv. Model. Earth Syst.* **8** (1), 3–30.
- HOLT, S. E., KOSEFF, J. R. & FERZIGER, J. H. 1992 A numerical study of the evolution and structure of homogeneous stably stratified sheared turbulence. *J. Fluid Mech.* **237**, 499–539.
- HUANG, J. & BOU-ZEID, E. 2013 Turbulence and vertical fluxes in the stable atmospheric boundary layer. Part I: a large-eddy simulation study. *J. Atmos. Sci.* **70** (6), 1513–1527.
- VAN HOOIJDONK, I. G. S., CLERCX, H. J. H., ANSORGE, C., MOENE, A. F. & VAN DE WIEL, B. J. H. 2018 Parameters for the collapse of turbulence in the stratified plane Couette flow. *J. Atmos. Sci.* **75**, 3211–3231.
- ISAZA, J. C. & COLLINS, L. R. 2009 On the asymptotic behaviour of large-scale turbulence in homogeneous shear flow. *J. Fluid Mech.* **637**, 213–239.
- JACOBITZ, F. G., SARKAR, S. & VANATTA, C. W. 1997 Direct numerical simulations of the turbulence evolution in a uniformly sheared and stably stratified flow. *J. Fluid Mech.* **342**, 231–261.
- KADER, B. A. & YAGLOM, A. M. 1990 Mean fields and fluctuation moments in unstably stratified turbulent boundary-layers. *J. Fluid Mech.* **212**, 637–662.
- KARIMPOUR, F. & VENAYAGAMOORTHY, S. K. 2015 On turbulent mixing in stably stratified wall-bounded flows. *Phys. Fluids* **27** (4), 046603.
- KATUL, G. G., KONINGS, A. G. & PORPORATO, A. 2011 Mean velocity profile in a sheared and thermally stratified atmospheric boundary layer. *Phys. Rev. Lett.* **107** (26), 268502.
- KATUL, G. G., PORPORATO, A., MANES, C. & MENEVEAU, C. 2013 Co-spectrum and mean velocity in turbulent boundary layers. *Phys. Fluids* **25** (9), 91702.
- KATUL, G. G., PORPORATO, A., SHAH, S. & BOU-ZEID, E. 2014 Two phenomenological constants explain similarity laws in stably stratified turbulence. *Phys. Rev. E* **89** (2), 023007.
- KEITZL, T., MELLADO, J. P. & NOTZ, D. 2016 Impact of thermally driven turbulence on the bottom melting of ice. *J. Phys. Oceanogr.* **46** (4), 1171–1187.
- LAUNDER, B. E., REECE, G. J. & RODI, W. 1975 Progress in the development of a Reynolds-stress turbulence closure. *J. Fluid Mech.* **68** (3), 537–566.
- LI, D. & BOU-ZEID, E. 2011 Coherent structures and the dissimilarity of turbulent transport of momentum and scalars in the unstable atmospheric surface layer. *Boundary-Layer Meteorol.* **140** (2), 243–262.
- LI, D., KATUL, G. G. & LIU, H. 2018 Intrinsic constraints on asymmetric turbulent transport of scalars within the constant flux layer of the lower atmosphere. *Geophys. Res. Lett.* **45** (4), 2022–2030.
- LI, D., SALESKY, S. T. & BANERJEE, T. 2016 Connections between the Ozmidov scale and mean velocity profile in stably stratified atmospheric surface layers. *J. Fluid Mech.* **797**, R3.
- MAHRT, L. 2014 Stably stratified atmospheric boundary layers. *Annu. Rev. Fluid Mech.* **46** (1), 23–45.
- MCCOLL, K. A., KATUL, G. G., GENTINE, P. & ENTEKHABI, D. 2016 Mean-velocity profile of smooth channel flow explained by a cospectral budget model with wall-blockage. *Phys. Fluids* **28** (3), 035107.
- MELLADO, J. P. 2012 Direct numerical simulation of free convection over a heated plate. *J. Fluid Mech.* **712**, 418–450.
- MELLOR, G. L. & YAMADA, T. 1982 Development of a turbulence closure model for geophysical fluid problems. *Rev. Geophys.* **20** (4), 851–875.
- MILES, J. W. & HOWARD, L. N. 1964 Note on a heterogeneous shear flow. *J. Fluid Mech.* **20** (2), 331–336.

- MOENG, C. 1984 A large-eddy-simulation model for the study of planetary boundary-layer turbulence. *J. Atmos. Sci.* **41** (13), 2052–2062.
- MOMEN, M. & BOU-ZEID, E. 2017 Mean and turbulence dynamics in unsteady Ekman boundary layers. *J. Fluid Mech.* **816**, 209–242.
- MONIN, A. S. & OBUKHOV, A. M. 1954 Basic laws of turbulent mixing in the ground layer of the atmosphere. *Akad. Nauk. SSSR. Geofiz. Inst. Trudy* **151**, 163–187.
- POPE, S. B. 2000 *Turbulent Flows*. Cambridge University Press.
- PUMIR, A. 1996 Turbulence in homogeneous shear flows. *Phys. Fluids* **8** (11), 3112–3127.
- SALESKY, S. T., CHAMECKI, M. & BOU-ZEID, E. 2017 On the nature of the transition between roll and cellular organization in the convective boundary layer. *Boundary-Layer Meteorol.* **163** (1), 41–68.
- SALESKY, S. T., CHAMECKI, M. & DIAS, N. L. 2012 Estimating the random error in eddy-covariance based fluxes and other turbulence statistics: the filtering method. *Boundary-Layer Meteorol.* **144** (1), 113–135.
- SHAH, S. K. & BOU-ZEID, E. 2014a Direct numerical simulations of turbulent Ekman layers with increasing static stability: modifications to the bulk structure and second-order statistics. *J. Fluid Mech.* **760**, 494–539.
- SHAH, S. & BOU-ZEID, E. 2014b Very-large-scale motions in the atmospheric boundary layer deduced by snapshot proper orthogonal decomposition. *Boundary-Layer Meteorol.* **153** (3), 355–387.
- SPALART, P. R. 1988 Direct simulation of a turbulent boundary-layer up to $R_\theta = 1410$. *J. Fluid Mech.* **187**, 61–98.
- STULL, R. B. 1988 *An Introduction to Boundary Layer Meteorology*. Kluwer Academic Publishers.
- VENAYAGAMOORTHY, S. K. & KOSEFF, J. R. 2016 On the flux Richardson number in stably stratified turbulence. *J. Fluid Mech.* **798**, R1.
- WYNGAARD, J. C. 2010 *Turbulence in The Atmosphere*. Cambridge University Press.
- YAMADA, T. 1975 The critical Richardson number and the ratio of the eddy transport coefficients obtained from a turbulence closure model. *J. Atmos. Sci.* **32** (5), 926–933.
- YOU, J., YOO, J. Y. & CHOI, H. 2003 Direct numerical simulation of heated vertical air flows in fully developed turbulent mixed convection. *Intl J. Heat Mass Transfer* **46** (9), 1613–1627.
- ZILITINKEVICH, S. 2002 Third-order transport due to internal waves and non-local turbulence in the stably stratified surface layer. *Q. J. R. Meteorol. Soc.* **128** (581), 913–925.
- ZILITINKEVICH, S. S. 1973 Shear convection. *Boundary-Layer Meteorol.* **3** (4), 416–423.